aerospace

MDPI

Article

Design of a Maglev Stewart Platform for the Microgravity Vibration Isolation

He Ma [1], Weichao Chi [1,*], Caihua Wang [1] and Jia Luo [2]

[1] Key Laboratory of Structural Dynamics of Liaoning Province, College of Sciences, Northeastern University, Shenyang 110819, China
[2] Beijing Institute of Structure and Environment Engineering, Beijing 100076, China
* Correspondence: chiweichao@gmail.com

Abstract: Vibration isolation mechanisms are usually installed on spacecraft between the vibration sources and the payload to ensure that precision instruments work properly. This paper proposes a novel maglev Stewart platform for vibration isolation in a microgravity environment. The maglev Stewart platform combines the quasi-zero stiffness of maglev actuators and the high maneuverability of the Stewart platform. The dynamic of the legs and the payload platform is analyzed, and the linear active disturbance rejection control (LADRC) algorithm is used to decouple the legs and cancel the total disturbance in the linear feedback. The simulation studies show that with the maglev Stewart platform, there is no longer any obvious resonance. The transmission ratio of vibration can be reduced significantly compared with the traditional elastic Stewart platform. Last but not least, the influence of two control parameters on vibration isolation performance is connected to certain physical meaning of the vibration problem.

Keywords: maglev actuator; Stewart platform; LADRC; microgravity vibration isolation

check for updates

Citation: Ma, H.; Chi, W.; Wang, C.; Luo, J. Design of a Maglev Stewart Platform for the Microgravity Vibration Isolation. *Aerospace* **2022**, *9*, 514. https://doi.org/10.3390/aerospace9090514

Academic Editor: Hekmat Alighanbari

Received: 30 July 2022
Accepted: 13 September 2022
Published: 15 September 2022

1. Introduction

Vibration isolation platforms have been extremely important to spacecraft as the demand of high-precision payloads for undisturbed environments has grown. Spacecraft in the microgravity environment are always interfered with by a variety of disturbances, including the rotation of attitude actuators, the flutter of solar panels, and thermal effects of the structure, etc. The performance of specific detection or communication tasks is guaranteed by vibration isolation platforms [1,2].

Traditional passive vibration isolation uses the combination of mass, spring, and damper. It is usually sufficient for high-frequency vibration isolation, and it does not need any power. Although they have the advantages of high reliability and low cost, passive vibration isolation devices have an unavoidable compromise between stiffness and vibration isolation performance [3,4]. Active vibration isolation has been used to compensate for the shortcomings in passive damping methods. By providing real-time varying force according to the sensor's feedback, active isolation can reduce the vibration transmission and make significant attenuation over passive methods. The active vibration isolation technology has become more mature with the development of actuators, sensors, and computer control systems. Early in 1996, Fuller et al. introduced vibration isolation systems using the concept of feedforward and feedback [5]. Preumont et al. used the root locus method on a skyhook isolator with force and acceleration feedback [6].

In most circumstances, the passive and active methods are used together in vibration isolation, to combine the advantages of the two achievements. This is classified as hybrid vibration isolation. A variety of different mechanisms have been developed to realize multiple-degree-of-freedom (MDOF) hybrid vibration isolation. Among them, the Stewart platform, first proposed by Stewart as a six-degree-of-freedom flight simulator [7], has been used as an effective six degrees-of-freedom (DOF) active vibration isolation mechanism for its ability of attitude maneuvering. A general Stewart platform is shown as Figure 1. It consists of six extensible legs with actuators connecting the payload-platform to the base with joints. If the legs are perpendicular to adjacent legs, the mechanism become a "cubic" form, and the coupling effect is reduced [8]. Wu et al. proposed a new decoupling condition of stiffness matrix and designed an active micro-vibration isolation manipulator with voice coil motors as the actuator [9]. Chi et al. used linear active disturbance rejection control on a Stewart platform for vibration isolation for spacecraft [10].

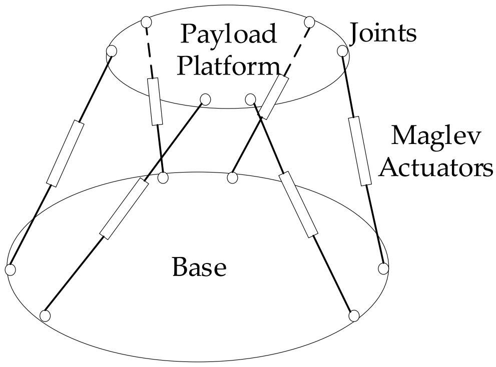

Figure 1. Structure diagram of a classical Stewart platform.

In the passive and hybrid vibration isolation structures, the additional stiffness is introduced to support the payload weight and isolate the vibration at the same time, but it may also introduce extra resonance at multiple frequencies. A kind of non-contacting maglev support, such as the maglev actuator, supports the payload weight with Lorentz force. It makes the mover floating over the stator with zero stiffness, so the path for vibration transmission is cut off. In view of the characteristics of zero stiffness, no friction, and large stroke, maglev actuators have been researched for applications in aerospace [11,12]. Long et al. developed a single DOF magnetic suspension active vibration isolation platform, adopted a hybrid vibration isolation on a prototype, and tested vibration isolation performance by experiments [13]. Shi et al. improved a maglev inertially stabilized platform (MISP) equipped with magnetic bearings instead of mechanical bearings and designed active vibration control method for the MISP [14].

Whether it is hybrid vibration isolation or maglev vibration isolation, the actuator needs to give appropriate real-time actuation force. A certain control algorithm has to be used to determine the actuation force by pole configuration or other means for control system design. Gáspár et al. described the various uncertainties in vibration isolation structures mathematically and designed a robust control system [15]. Zhang et al. used H∞ vibration control for flexible linkage mechanism systems [16]. Gao presented a method of tuning the parameters of linear feedback and extended state observer under the concept of bandwidth, which relate theoretical control parameters to practical physical meaning [17]. Zhao et al. used the active disturbance rejection control (ADRC) on a two-inertia vibration system by assuming the resonance to be unknown and treated it as disturbance [18].

In this paper, a novel maglev Stewart platform and the active vibration isolation control algorithm are presented. The design utilizes the strong attitude actuation ability of the Stewart platform and has a large vibration isolation stroke and uses the maglev design to avoid the resonance introduced by the traditional spring support. To focus on the attitude stability control, it is assumed that the mechanism can be suspended with a constant current in the coil and the initial state of the actuators are at the middle stroke. The linear active disturbance rejection control (LADRC) algorithm is used to provide quasi-zero stiffness by adjusting the length of the legs in real time.

This paper is organized as follows. The design and configuration of maglev platform is given in Section 2. The control formula of the Stewart platform is established in Section 3. The LADRC control strategy for the multi-input multi-output (MIMO) system is presented in Section 4, which is verified by several numerical simulation results.

2. Configuration of Maglev Platform

2.1. Actuator

The mechanism of the maglev actuator, which consists of a stator and a mover, is shown in Figure 2. The stator has a cylindrical permanent magnet installed in the center of a ferromagnetic yoke. A cylindrical ferromagnetic yoke is installed at the other end of the permanent magnet. The stator provides a uniform radially oriented magnetic field in the annular air gap and constrains the relative motion between the mover and the stator to be linear motion by a linear bearing. The mover has a tubular coil wound on the sleeve and situated in the magnetic field. When the coil is energized, an Ampere force will be generated on the coil perpendicular to the magnetic flux and the current flow according to the Ampere Force Principle.

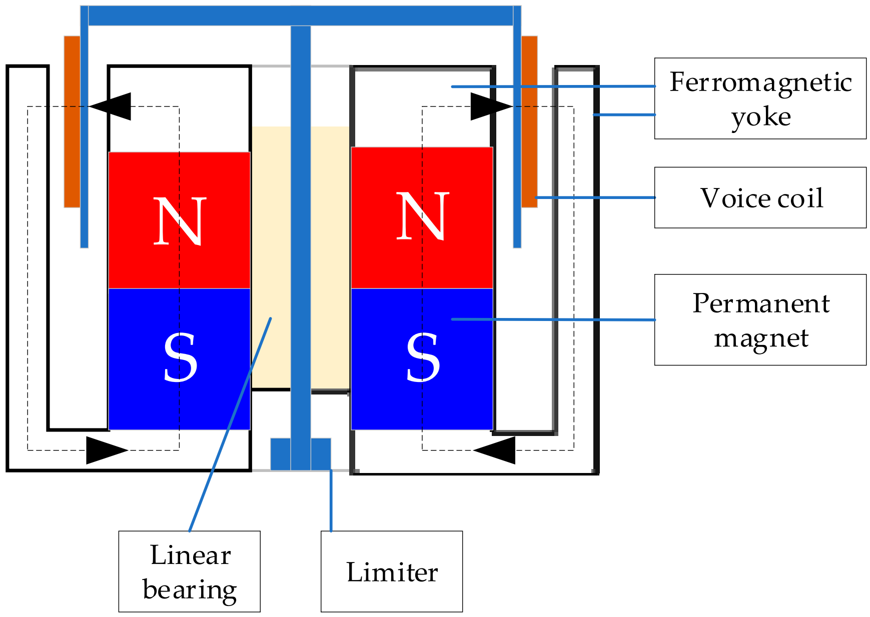

Figure 2. Cross-sectional diagram of the maglev actuator.

If we consider the flux lines in the air gap on the cross-section through the axis, it is found that the flux lines are parallel and uniform, so the maglev actuator can provide a linear force proportional to current, magnetic flux density, and coil length in the magnetic field even if the coil is moving in the axial direction. In the case of a bent wire with a steady current I, the force acting on the mover is calculated as

$$k_M F = \oint_L i d\mathbf{l} \times \mathbf{B} = Bli = k_M i \tag{1}$$

where l is the length of the coil in the magnetic field, in the same direction as current i; B is the magnetic induction; k_M is known as the electromagnetic constant. The current I can be obtained when a target force F is given. If the ampere force is exactly equal to the gravity of the load, then the load is suspended in the air under the action of the electromagnetic force without spring support.

2.2. Platform

The maglev actuator presented above has a large stroke along the linear bearing, so theoretically it can isolate a large vibration or provide the attitude maneuver of the load. For 6-DOF missions, the actuators must be assembled into a proper mechanism. In this paper, the Stewart platform is utilized to realize the isolation and attitude maneuvering for its powerful capability of 6-DOF attitude adjustment.

The diagram of the maglev Stewart platform is shown in Figure 3. The platform is mainly composed of an upper platform and a base platform connected with six legs, each of which is equipped with a maglev actuator. Because of the constraint of the liner bearing, each leg can only change its length while rotating around the spherical joints fixed to the upper and base platforms. When current is distributed to the coil of each actuator, force for maglev and 6-DOF movement is generated on each leg. The maglev Stewart platform can be used for vibration isolation as well as for motion tracking of the payload installed on the upper platform. The main parameters of the maglev Stewart platform prototype are presented in Table 1.

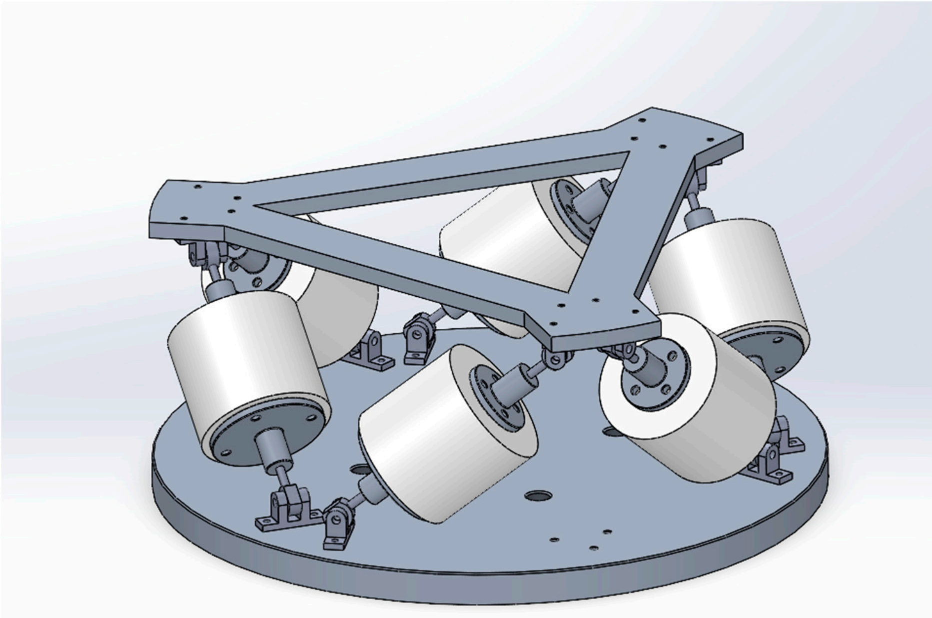

Figure 3. The design of the maglev Stewart platform.

Table 1. Main specifications of the maglev Stewart platform.

Specification	Value
Payload mass	4.85 kg
Top platform mass	3.29 kg
Base platform radius	0.165 m
Platform height	0.079 m
Leg length	0.162 m
Leg length variation range	± 0.01 m
Top platform moment of inertia	$diag(4.1, 4.4, 8) \times 10^{-2}$ kg·m^2

3. Modeling of the Vibration Isolation Structure

3.1. Reference Frames Definitions

To transform all vectors into an inertial coordinate system for description and calculation, we define the local coordinate frames B, P, D_{i}, and U_{i}, which are attached to the base platform, the payload platform, the ith lower leg, and the ith upper leg, respectively. The inertial frame and the local frames are shown in Figure 4.

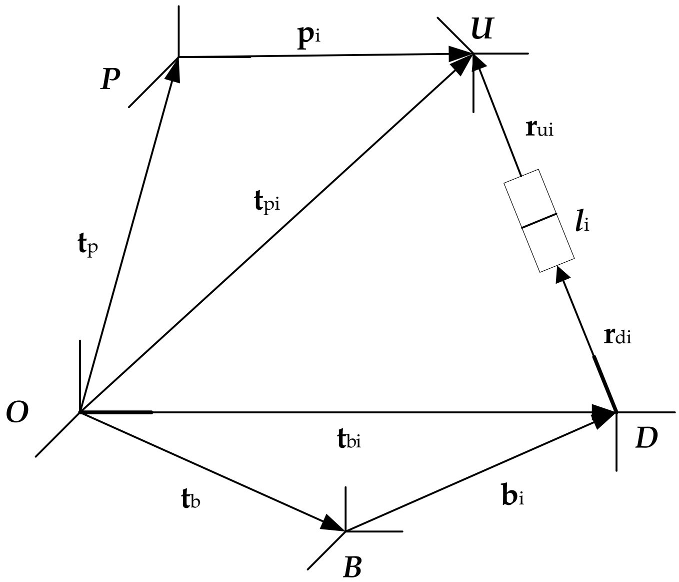

Figure 4. The inertial frame and the local frames.

3.2. Kinematics and Dynamics of the Legs

This section studies the influence of the dynamic characteristics of the maglev legs on the system performance. According to the relationship of the frames, the position vectors of the ends of the *i*th leg can be expressed as

$$\mathbf{t}_{pi} = \mathbf{t}_p + \mathbf{p}_i \tag{2}$$

$$\mathbf{t}_{bi} = \mathbf{t}_b + \mathbf{b}_i \tag{3}$$

where $\mathbf{t}_b$ and $\mathbf{t}_p$ are the position vectors of B and P, the mass center of base platform and upper platform, in the inertial frame O. The legs vector can be obtained by subtracting (2) and (3):

$$\mathbf{l}_i = \mathbf{t}_{pi} - \mathbf{t}_{bi} = \left(\mathbf{t}_p + \mathbf{p}_i\right) - \left(\mathbf{t}_b + \mathbf{b}_i\right) \tag{4}$$

Differentiating the above formula, we get the velocity of the *i*th leg as

$$\dot{\mathbf{l}}_i = \left(\dot{\mathbf{t}}_{pi} - \dot{\mathbf{t}}_{bi}\right)\cdot\boldsymbol{\tau}_i = \begin{bmatrix}\boldsymbol{\tau}_i^{\mathrm{T}} & (\mathbf{p}_i \times \boldsymbol{\tau}_i)^{\mathrm{T}}\end{bmatrix}\begin{bmatrix}\dot{\mathbf{t}}_p \\ \boldsymbol{\omega}_p\end{bmatrix} - \begin{bmatrix}\boldsymbol{\tau}_i^{\mathrm{T}} & (\mathbf{b}_i \times \boldsymbol{\tau}_i)^{\mathrm{T}}\end{bmatrix}\begin{bmatrix}\dot{\mathbf{t}}_b \\ \boldsymbol{\omega}_b\end{bmatrix} \tag{5}$$

where $\boldsymbol{\tau}_i = \mathbf{l}_i / l_i$ is a unit vector along the direction of $\mathbf{l}_i$; $\boldsymbol{\omega}_p$, $\boldsymbol{\omega}_b$ are the angular velocity of the upper platform and the base; and $\dot{\mathbf{t}}_{pi}$ and $\dot{\mathbf{t}}_{bi}$ are the velocity of the upper leg and lower leg.

The derivative of the six lengths of legs to time can be obtained from Equation (5) as

$$\dot{\mathbf{l}} = \mathbf{H}_p^{\mathrm{T}}\begin{bmatrix}\dot{\mathbf{r}}_p \\ \boldsymbol{\omega}_p\end{bmatrix} - \mathbf{H}_b^{\mathrm{T}}\begin{bmatrix}\dot{\mathbf{r}}_b \\ \boldsymbol{\omega}_b\end{bmatrix} \tag{6}$$

where

$$\mathbf{H}_p = \begin{bmatrix}\boldsymbol{\tau}_1 & \cdots & \boldsymbol{\tau}_6 \\ \mathbf{p}_1 \times \boldsymbol{\tau}_1 & \cdots & \mathbf{p}_6 \times \boldsymbol{\tau}_6\end{bmatrix},\ \mathbf{H}_b = \begin{bmatrix}\boldsymbol{\tau}_1 & \cdots & \boldsymbol{\tau}_6 \\ \mathbf{b}_1 \times \boldsymbol{\tau}_1 & \cdots & \mathbf{b}_6 \times \boldsymbol{\tau}_6\end{bmatrix} \tag{7}$$

The force that acts between the upper and the lower legs is

$$\mathbf{F} = -\mathbf{C}\dot{\mathbf{l}} + \mathbf{F}_a = -\mathbf{C}\mathbf{H}_p^{\mathrm{T}}\begin{bmatrix}\dot{\mathbf{r}}_p \\ \boldsymbol{\omega}_p\end{bmatrix} + \mathbf{C}\mathbf{H}_b^{\mathrm{T}}\begin{bmatrix}\dot{\mathbf{r}}_b \\ \boldsymbol{\omega}_b\end{bmatrix} + \mathbf{F}_a \tag{8}$$

where $\mathbf{F}_a = \begin{bmatrix} F_{a1} & \cdots & F_{a6} \end{bmatrix}^{\mathrm{T}}$ is the force vector of the maglev actuators; and $\mathbf{C}$ is the counter electromotive force damping coefficient on each actuator.

3.3. Differential Equation of Motion for the Payload Platform

The free body diagram of the payload platform is shown in Figure 5. Here, M_P is the total mass, $\mathbf{a}_{\mathrm{p}}$ is the mass center acceleration, and $\mathbf{F}_w$ and $\mathbf{M}_w$ are external force and torque, respectively. According to Newton's dynamical law, the payload platform satisfies the following expression:

$$\mathbf{F}_w + \sum_{i=1}^{6} \mathbf{F}_{ui} = M_p \mathbf{a}_p \tag{9}$$

where

$$\mathbf{a}_p = \ddot{\mathbf{t}}_p + \boldsymbol{\alpha}_p \times \mathbf{r} + \boldsymbol{\omega}_p \times (\boldsymbol{\omega}_p \times \mathbf{r}) \tag{10}$$

where $\mathbf{r}$ is the position vector of the mass center. For the upper platform and the payload, we have

$$-\sum_{i=1}^{6} \mathbf{p}_i \times \mathbf{F}_{ui} + \sum_{i=1}^{6} \mathbf{f}_i + \mathbf{M}_w = \boldsymbol{\omega}_p \times \mathbf{I}_p^* \boldsymbol{\omega}_p + \mathbf{I}_p^* \boldsymbol{\alpha}_p \tag{11}$$

according to Euler equation. Here, $\mathbf{f}_i$ is the force of the maglev actuators, and

$$\mathbf{I}_p^* = \mathbf{I}_p + M_p \left(\mathbf{r}^T \mathbf{r} E_3 - \mathbf{r}\mathbf{r}^T \right) \tag{12}$$

From Equations (9) and (11), ignoring higher order infinitesimals in the derivation, we have

$$\mathbf{J}_p \begin{bmatrix} \ddot{\mathbf{t}}_p \\ \boldsymbol{\alpha}_p \end{bmatrix} = \mathbf{J}_b \begin{bmatrix} \ddot{\mathbf{t}}_b \\ \boldsymbol{\alpha}_b \end{bmatrix} + \mathbf{H}_p \mathbf{F} + \begin{bmatrix} \mathbf{F}_w + M_p \mathbf{g} \\ -\mathbf{M}_w - M_p \mathbf{r} \times \mathbf{g} \end{bmatrix} \tag{13}$$

where we denote that

$$\mathbf{J}_b = \sum_{i=1}^{6} \begin{bmatrix} \mathbf{Q}_{pi} & -\mathbf{Q}_{pi} \tilde{\mathbf{b}}_i \\ -\tilde{\mathbf{p}}_i \mathbf{Q}_{pi} & \tilde{\mathbf{p}}_i \mathbf{Q}_{pi} \tilde{\mathbf{b}}_i \end{bmatrix} \tag{14}$$

$$\mathbf{J}_p = \begin{bmatrix} M_p \mathbf{E}_3 & -M_p \tilde{\mathbf{r}} \\ 0 & \mathbf{I}_p^* \end{bmatrix} + \sum_{i=1}^{6} \begin{bmatrix} \mathbf{Q}_{pi} & -\mathbf{Q}_{pi} \tilde{\mathbf{p}}_i \\ -\tilde{\mathbf{p}}_i \mathbf{Q}_{pi} & \tilde{\mathbf{p}}_i \mathbf{Q}_{pi} \tilde{\mathbf{p}}_i \end{bmatrix} \tag{15}$$

$$\begin{aligned} \mathbf{Q}_{pi} = \; & m_{ui} \boldsymbol{\tau}_i \boldsymbol{\tau}_i^{\mathrm{T}} \\ & + \frac{\left(\mathbf{E}_3 - \boldsymbol{\tau}_i \boldsymbol{\tau}_i^{\mathrm{T}}\right)}{(2l_{ui} + 2l_{ui} - l_i) l_i} \left[m_{ui} \kappa_i (l_i - l_{ui}) + m_{di} l_{di}^2 \right] \\ & - \frac{1}{(2l_{ui} + 2l_{ui} - l_i)_i l_i} \tilde{\boldsymbol{\tau}}_i (\mathbf{I}_{di} + \mathbf{I}_{ui}) \tilde{\boldsymbol{\tau}}_i \end{aligned} \tag{16}$$

$$\mathbf{Q}_{bi} = \frac{\left(\mathbf{E}_3 - \boldsymbol{\tau}_i \boldsymbol{\tau}_i^{\mathrm{T}}\right)}{(2l_{ui} + 2l_{ui} - l_i)_i l_i} \left[m_{di} l_{di} + m_{ui} \kappa_i l_{ui} \right] - \frac{1}{(2l_{ui} + 2l_{ui} - l_i) l_i} \tilde{\boldsymbol{\tau}}_i (\mathbf{I}_{di} + \mathbf{I}_{ui}) \tilde{\boldsymbol{\tau}}_i \tag{17}$$

where the "~" denotes the transformation of the vector $\mathbf{a} = \begin{bmatrix} a_1 & a_2 & a_3 \end{bmatrix}^{\mathrm{T}}$ to

$$\tilde{\mathbf{a}} = \begin{bmatrix} 0 & -a_3 & a_2 \\ a_3 & 0 & -a_1 \\ -a_2 & a_1 & 0 \end{bmatrix} \tag{18}$$

Finally, the task-space equation can be obtained from (13) as

$$\mathbf{J}_p \ddot{\mathbf{x}}_p + \mathbf{H}_p \mathbf{C} \mathbf{H}_p^{\mathrm{T}} \dot{\mathbf{x}}_p = \mathbf{J}_b \ddot{\mathbf{x}}_b + \mathbf{H}_p \mathbf{C} \mathbf{H}_b^{\mathrm{T}} \dot{\mathbf{x}}_b + \mathbf{H}_p \mathbf{F}_a + \begin{bmatrix} \mathbf{F}_w + M_p \mathbf{g} \\ -\mathbf{M}_w - M_p \mathbf{r} \times \mathbf{g} \end{bmatrix} \tag{19}$$

where the generalized coordinates are defined as

$$\mathbf{x}_p = \begin{bmatrix} \mathbf{t}_p \\ \theta_p \end{bmatrix}, \mathbf{x}_b = \begin{bmatrix} \mathbf{t}_b \\ \theta_b \end{bmatrix} \tag{20}$$

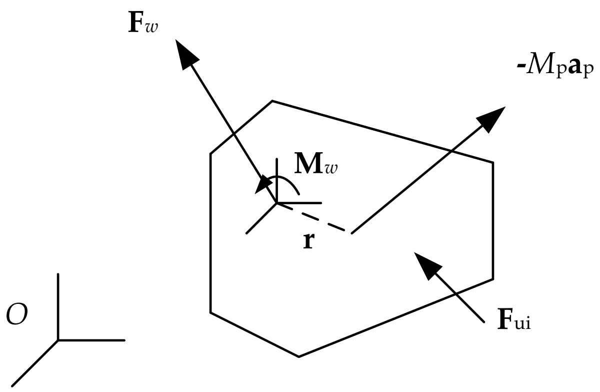

Figure 5. Free body diagram of the payload platform.

4. Control System Design and Simulation Study

4.1. LADRC Design for the Stewart Platform

Due to the mass and moment of inertia of the legs, the motion of the upper platform is not zero stiffness unless extra control forces are exerted by the maglev actuators. The active control system drives the legs, changing their lengths to make the platform equivalently quasi-zero stiffness. Model nonlinearity and unmodeled dynamics, such as the magnetic field of the maglev actuators and the dynamic of the cables, have a great influence on the active vibration isolation. As shown in Equation (19), the platform is a nonlinear dynamic system under external forces and disturbance from the base. The dynamic of each leg is also highly coupled. This paper employs LADRC to eliminate disturbances and various uncertainties.

By generalizing the disturbance as the total disturbance, the LADRC estimates the model uncertainties and model coupling with the linear extended state observer (LESO) and the linear feedback to reject the total disturbance. The final control vector is obtained with the linear combination of the state errors and the generalized disturbance. The diagram of LADRC for a MIMO system is shown in Figure 6.

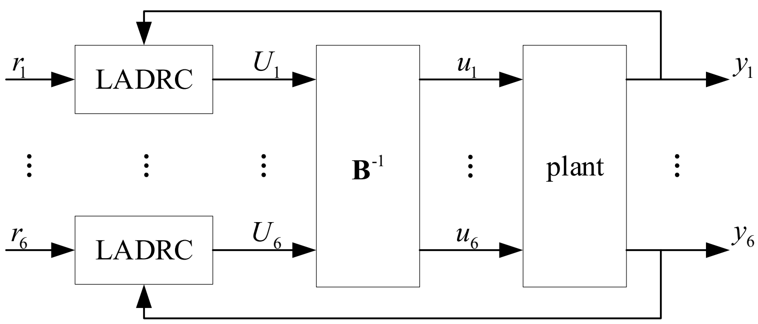

Figure 6. The diagram of LADRC for a MIMO system.

We rewrite Equation (19) as the following general form of series integral form with perturbation term

$$\begin{cases} \ddot{\mathbf{x}} = \mathbf{f}(x, \dot{x}, w, \dot{w}, t) + \mathbf{Bu} \\ \mathbf{y} = \mathbf{x} \end{cases} \tag{21}$$

where $\mathbf{x} = \begin{bmatrix} x_1 & \cdots & x_6 \end{bmatrix}^{\mathrm{T}}$ is the generalized coordinate vector, $\mathbf{f} = \begin{bmatrix} f_1 & \cdots & f_6 \end{bmatrix}^{\mathrm{T}}$ is the total disturbance, $\mathbf{B} = \mathbf{J}_p^{-1}\mathbf{H}_p = \begin{bmatrix} b_{11} & \cdots & b_{16} \\ \vdots & \vdots & \vdots \\ b_{61} & \cdots & b_{66} \end{bmatrix}$ $\mathbf{u} = \begin{bmatrix} u_1 & \cdots & u_6 \end{bmatrix}^{\mathrm{T}}$ is the control vector, and $\mathbf{B}$ is the control matrix of the Stewart platform, where

$$\mathbf{B} = \mathbf{J}_p^{-1}\mathbf{H}_p = \begin{bmatrix} b_{11} & \cdots & b_{16} \\ \vdots & \vdots & \vdots \\ b_{61} & \cdots & b_{66} \end{bmatrix} \quad (22)$$

For a single channel, the above relationship between the states comes into

$$\begin{cases} \ddot{x}_i = f_i(x, \dot{x}, \cdots, x_6, \dot{x}_6, t) + U_i \\ y_i = x_i \end{cases} \quad (23)$$

Here we define U_{i} as the virtual control variable, for it is not the exact control force. It can be seen that U_{i} and y_{i} are completely decoupled. The actual control force, $\mathbf{u} = \begin{bmatrix} u_1 & \cdots & u_6 \end{bmatrix}^{\mathrm{T}}$, is determined by the virtual control vector $\mathbf{U}$ from

$$\mathbf{u} = \mathbf{B}^{-1}\mathbf{U} \quad (24)$$

where $\mathbf{U} = \begin{bmatrix} U_1 & \cdots & U_6 \end{bmatrix}$. Then the control problem for MIMO system can be realized by six channels in parallel. The next key point is to cancel the total disturbance in each channel and make each control system in (23) a series integral system.

Generally, consider a second order control system given as

$$\ddot{y} + a_1\dot{y} + a_2 y = b_1\ddot{w} + b_2\dot{w} + b_3 w + bu \quad (25)$$

where y, w, and u represent the output, external disturbance, and control force of the mechanism, respectively; a_1, a_2, b_1, b_2, b_3, and b are the coefficients of the dynamic system. We arrange Equation (25) into the following form:

$$\ddot{y} = -a_1\dot{y} - a_2 y + b_1\ddot{w} + b_2\dot{w} + b_3 w + (b - b_0)u + b_0 u \quad (26)$$

The expression of $\ddot{y}$ consists of two parts, denoted by

$$f_1 = -a_1\dot{y} - a_2 y + (b - b_0)u \quad (27)$$

and

$$f_2 = b_1\ddot{w} + b_2\dot{w} + b_3 w \quad (28)$$

Here, f_1 is the internal dynamics and f_2 is the external disturbance. The total disturbance is presented with generalized disturbance f,

$$f = -a_1\dot{y} - a_2 y + b_1\ddot{w} + b_2\dot{w} + b_3 w + (b - b_0)u \quad (29)$$

which denotes the key point of the LADRC solution. Defining the state variables $x_1 = y$, $x_2 = \dot{x}_1$, $x_3 = f$, then (26) can be rewritten as

$$\begin{cases} \dot{x}_1 = x_2 \\ \dot{x}_2 = x_3 + b_0 u \\ \dot{x}_3 = \dot{f} \\ y = x_1 \end{cases} \quad (30)$$

where x_3 is known as the extended state.

To estimate the states and the generalized disturbance, we use an observer as

$$\begin{cases} e = y - z_1 \\ \dot{z}_1 = z_2 + \beta_1 e \\ \dot{z}_2 = z_3 + \beta_2 e + b_0 u \\ \dot{z}_3 = \beta_3 e \end{cases} \tag{31}$$

where z_1, z_2, z_3 denote the estimate of the corresponding states. The observer (31) can estimate an extra state compared to the Luenberger observer, so it is known as a linear extended state observer (LESO). The selection of the LESO gain β_1, β_2, and β_3 is similar to that of the Luenberger observer, by placing the observer poles in the left half-plane. Gao proposed a method of placing the observer poles at $-\omega_O$ to get the gain vector as

$$L = \begin{bmatrix} \beta_1 & \beta_2 & \beta_3 \end{bmatrix} = \begin{bmatrix} 3\omega_o & 3\omega_o^2 & \omega_o^3 \end{bmatrix} \tag{32}$$

and the only parameter can be tuned very easily in control engineering [13]. Here, ω_O is also the bandwidth of the observer, which can be tuned for better estimating performance, as well as the bandwidth of a low pass filter. With the LESO, all states and the total disturbance can be estimated and then used for a feedback linearization as

$$u = \frac{-z_3 + u_0}{b_0} \tag{33}$$

where the error feedback u_0 is an input variable. Substituting the feedback Equation (33) to the system (30), we have

$$\ddot{y} = \bar{e}_3 + u_0 \tag{34}$$

where the estimation error is $\bar{e}_3 = f - z_3$. Ignoring the estimation error, system (34) turns into a simple linear double-integrator as

$$\ddot{y} \approx u_0 \tag{35}$$

Let the input variable u_0 be

$$u_0 = k_p(r - z_1) - k_d z_2 \tag{36}$$

where r is the reference input of the control system. Similar to the LESO, the feedback parameters can also connect with the physical quantity by the concept of control bandwidth. By choosing the feedback parameters as

$$k_d = 2\xi\omega_c, k_p = \omega_c^2, \tag{37}$$

all closed-loop poles are placed at $-\omega_c$ which makes the system stable and meet certain dynamic performance. Here, ξ is the damping ratio. Let the control signal be

$$u = -\frac{k_p}{b_0}z_1 - \frac{k_d}{b_0}z_2 - \frac{1}{b_0}z_3 + \frac{k_p}{b_0}r \tag{38}$$

The total disturbance involving the disturbance and the uncertainties is estimated and canceled, and the system output y can track the reference signal, while the platform does not need to be mathematically detailed.

4.2. Numerical Simulation Studies

To evaluate the vibration isolation performance for the previous design, the maglev Stewart platform is simulated in Matlab (R2019b) from Mathworks and compared with the traditional Stewart platform with elastic legs. The structural parameters are listed in Table 1.

The frequency study linearizes the vibration isolation system with control and without control, which, respectively, represent the active and passive vibration isolation structure. The frequency response between the disturbance vector **w** and output vector **y** can reflect the performance and bandwidth of the vibration isolation system.

To simplify the diagram, only three of the six DOF are presented: disturbance and response of displacement along *x*-axis, *y*-axis, and *z*-axis; the correspondence between the three disturbances and the three responses is shown in Figure 7. In each diagram, the frequency response of the uncontrolled elastic platform, controlled elastic platform, uncontrolled maglev platform, and controlled maglev platform are presented in different colors.

From Figure 7, the maglev platform almost completely reduces the obvious resonance of the elastic platform, and, even if it is not controlled, the transmissibility of vibration is greatly attenuated compared with the elastic platform. Under the action of LADRC, the response has an attenuation up to 100 dB lower than that of the elastic platform with LADRC, which reflects the super vibration isolation ability of the maglev Stewart platform.

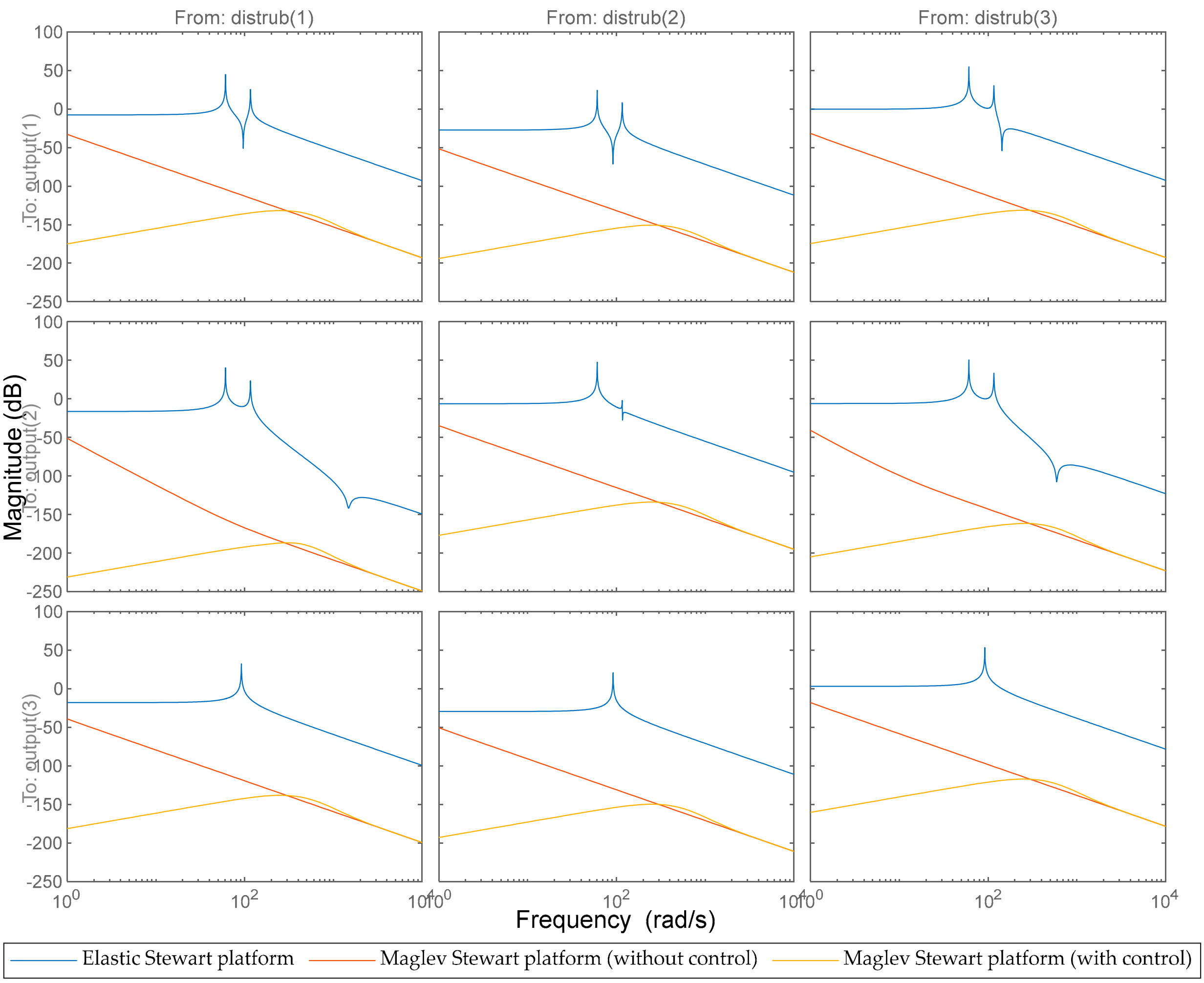

Figure 7. The frequency response from the base to the payload.

When focusing on the maglev Stewart platform, the control parameters ω_o and ω_c in LADRC also significantly influence the closed-loop frequency response. As shown in Figure 8, the curves in red, blue, orange, and purple represent the vibration transmission ratio with different parameters. It is shown that under LADRC, the vibration amplification at frequency lower than ω_o is attenuated significantly, whereas the vibration amplification at high frequency performs better than that of the elastic Stewart platform. The parameter ω_o, also known as the observer bandwidth, decides the bandwidth of the active vibration isolation and the cutoff frequency of the low pass filter. The controller bandwidth ω_c, in contrast, decides the amplitude of the transmissibility, which is a reflection of the position of closed-loop poles. It is also noticed that the controlled maglev Stewart platform is showing an increasing trend even above the uncontrolled case just near the cutoff frequency caused by the observer error.

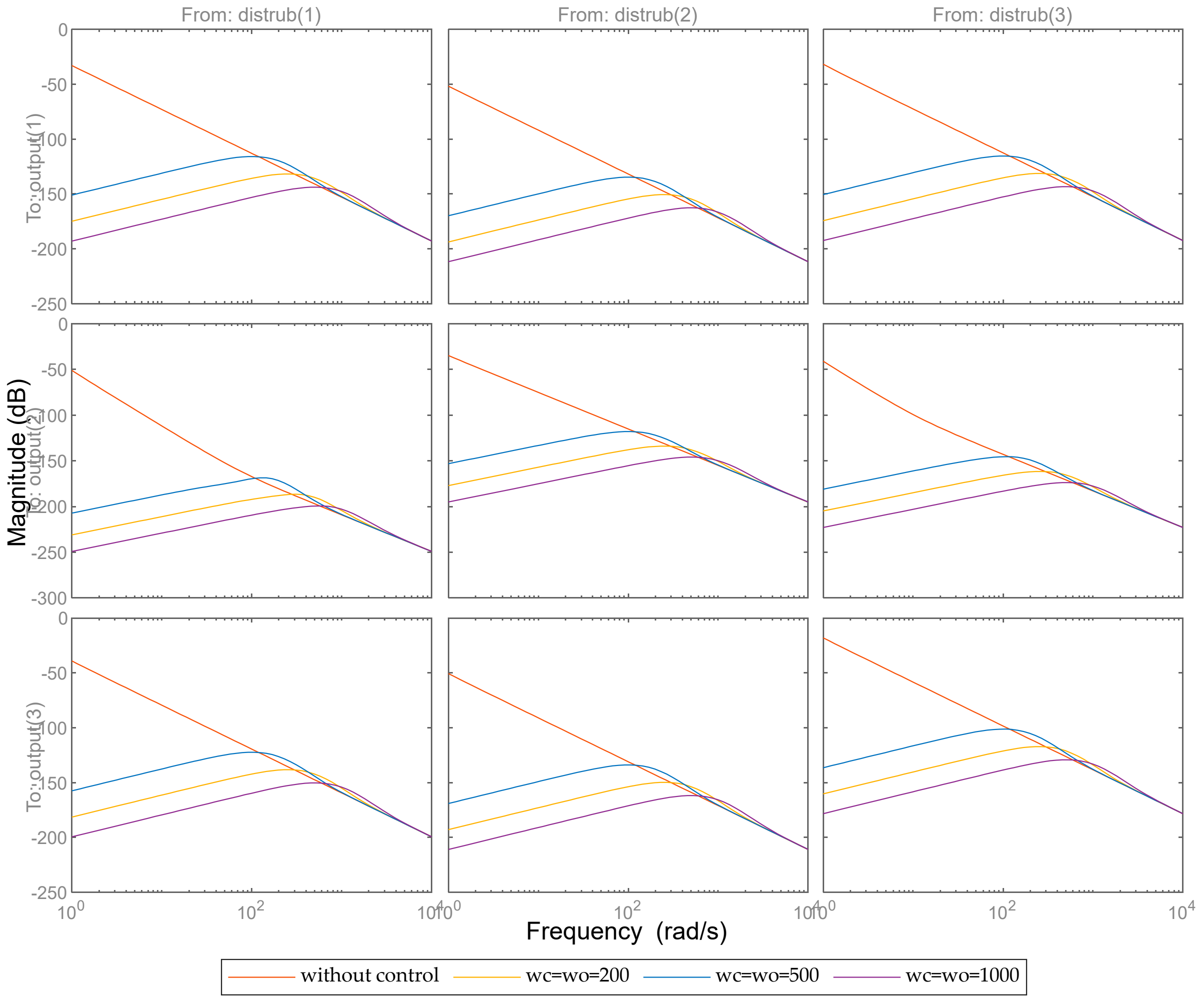

Figure 8. The frequency response from the base to the payload.

The time–domain response of the three displacements along the x, y, and z axes to the disturbance along x-axis is shown in Figure 9. The effectiveness of the LADRC method is evaluated through numerical simulation in Simulink. The same parameters are used as in the frequency response analysis. The sinusoidal disturbance is given at the base platform along the x-axis. The amplitude of the disturbance is 10^{-4} m and the frequency is the resonance frequency of the elastic Stewart platform, 60.6 rad/s. The figures show that the LADRC controller reduces the vibration response along the x-axis from 1.7×10^{-3} to 0.6×10^{-7}. The response of rotation angle around three axes perform similarly with different attenuating ranges.

Taking the above factors into consideration, when applying LADRC to the maglev Stewart platform for vibration isolation, the optimal control parameters should be chosen in a compromise between vibration amplitude attenuation and noise filtering if the sensor noise is within consideration in practical design.

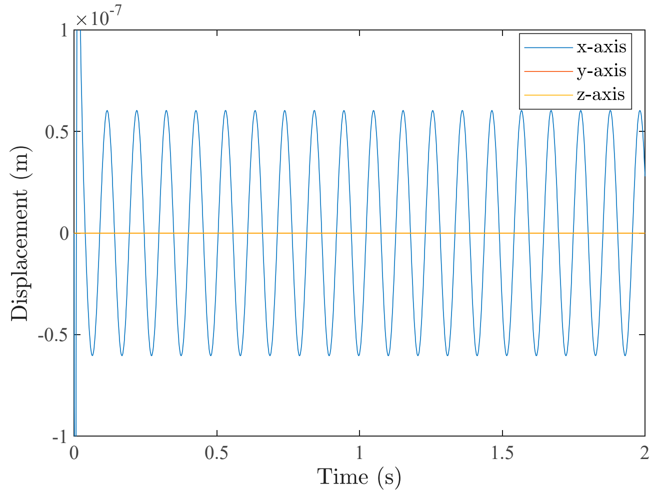

Figure 9. The time–domain response to the disturbance along the x-axis.

5. Conclusions

A novel design of a six DOF maglev Stewart platform for vibration isolation on spacecraft using LADRC is proposed in this paper. The configuration of the maglev actuator and the whole platform is described, and the dynamic model of the legs and the differential equation of motion for the upper platform are determined. From the six DOF coupled dynamic model, a LADRC solution is then presented by decoupling the MIMO system and canceling the total disturbance. The performance of the maglev platform is studied by simulation compared with the elastic Stewart platform and different control parameters. Results show that the maglev platform reduces the obvious resonance of the elastic platform significantly, either with or without control, but the properties with LADRC control is much closer to a quasi-zero stiffness vibration isolation system. With the LADRC, which is tuned according to the working frequencies, the maglev Stewart platform can attenuate the transmission of vibration for about 100 dB while having no resonance frequency at all, and the performance is also better than the elastic Stewart platform at high frequency. Influence of two control parameters ω_o and ω_c on vibration isolation performance is connected to certain physical meanings of the vibration isolation.

Author Contributions: Conceptualization, W.C. and J.L.; methodology, W.C.; software, W.C. and H.M.; validation, W.C., H.M. and C.W.; investigation, W.C.; writing—original draft preparation, W.C.; writing—review and editing, H.M. and J.L. All authors have read and agreed to the published version of the manuscript.

Funding: This research was supported by the National Natural Science Foundation of China (Grant No. 12002080).

Data Availability Statement: Not applicable.

Conflicts of Interest: The authors declare no conflict of interest.

References

1. Cao, D.Q.; Bai, K.C.; Ding, H.; Zhou, X.; Pan, Z.; Chen, L. Advances in dynamics and vibration control of large-scale flexible spacecraft. *Chin. J. Theor. Appl. Mech.* **2019**, *51*, 1–13.
2. Zhang, Y.; Zang, Y.; Li, M.; Wang, Y.; Li, W. Active-passive integrated vibration control for control moment gyros and its application to satellites. *J. Sound Vib.* **2017**, *394*, 1–14. [CrossRef]
3. Zhao, T.Y.; Ma, Y.; Zhang, H.Y.; Pan, H.G.; Cai, Y. Free vibration analysis of a rotating graphene nanoplatelet reinforced pre-twist blade-disk assembly with a setting angle. *Appl. Math. Model.* **2021**, *93*, 578–596. [CrossRef]
4. Zhao, T.Y.; Li, K.; Ma, H. Study on dynamic characteristics of a rotating cylindrical shell with uncertain parameters. *Anal. Math. Phys.* **2022**, *12*, 1–28. [CrossRef]
5. Fuller, C.C.; Elliott, S.J.; Nelson, P.A. *Active Control of Vibration*; Academic Press: Cambridge, MA, USA, 1996.

6. Preumont, A.; Francois, A.; Bossens, F.; Abu-Hanieh, A. Force feedback versus acceleration feedback in active vibration isolation. *J. Sound Vib.* **2002**, *257*, 605–613. [CrossRef]
7. Stewart, D. A platform with six degrees of freedom. *Proc. Inst. Mech. Eng.* **1965**, *180*, 371–386. [CrossRef]
8. Geng, Z.J.; Haynes, L.S. Six degree-of-freedom active vibration control using the Stewart platforms. *IEEE Trans. Control. Syst. Technol.* **1994**, *2*, 45–53. [CrossRef]
9. Wu, Y.; Yu, K.P.; Jiao, J.; Chi, W.; Tang, J. Dynamic isotropy design and analysis of a six-DOF active micro-vibration isolation manipulator on satellites. *Robot. Comput.-Integr. Manuf.* **2018**, *49*, 408–425. [CrossRef]
10. Chi, W.; Ma, S.; Sun, J. A hybrid multi-degree-of-freedom vibration isolation platform for spacecrafts by the linear active disturbance rejection control. *Appl. Math. Mech.* **2020**, *41*, 805–818. [CrossRef]
11. Zhu, T.; Cazzolato, B.; Robertson, W.S.P.; Zander, A. Vibration isolation using six degree-of-freedom quasi-zero stiffness magnetic levitation. *J. Sound Vib.* **2015**, *358*, 48–73. [CrossRef]
12. Kim, M.; Kim, H.; Gweon, D.-G. Design and optimization of voice coil actuator for six degree of freedom active vibration isolation system using Halbach magnet array. *Rev. Sci. Instrum.* **2012**, *83*, 105117. [CrossRef] [PubMed]
13. Long, Z.-Q.; Hao, A.-M.; Chen, G.; Long, Z. The research of active isolation platform with magnetically levitated control. *J. Astronaut.* **2003**, *24*, 510–514.
14. Shi, W.; Liu, K.; Zhao, W. Active Vibration Isolation of a Maglev Inertially Stabilized Platform Based on an Improved Linear Extended State Observer. *IEEE Access* **2021**, *9*, 743–751. [CrossRef]
15. Gáspár, P.; Szászi, I.; Bokor, J. Robust control design for mechanical systems using the mixed μ synthesis. *Period. Polytech. Transp. Eng.* **2003**, *30*, 37–52.
16. Zhang, X.; Shao, C.; Li, S.; Xu, D.; Erdman, A. Robust H∞ vibration control for flexible linkage mechanism systems with piezoelectric sensors and actuators. *J. Sound Vib.* **2001**, *243*, 145–155. [CrossRef]
17. Gao, Z.Q. Scaling and bandwidth-parameterization based controller tuning. In Proceedings of the American Control Conference, Denver, CO, USA, 4–6 June 2003; pp. 4989–4996.
18. Zhao, S.; Gao, Z. An Active Disturbance Rejection Based Approach to Vibration Suppression in Two-Inertia Systems. *Asian J. Control.* **2013**, *15*, 350–362. [CrossRef]